Designer Bloch plasmon polariton dispersion in grating-coupled hyperbolic metamaterials

Nicolò Maccaferri (iD), Tommi Isoniemi (iD), Michael Hinczewski (iD), Marzia Iarossi, Giuseppe Strangi (iD), and Francesco De Angelis (iD)

open access

View Online   Export Citation   CrossMark

Designer Bloch plasmon polariton dispersion in grating-coupled hyperbolic metamaterials

View Online   Export Citation   CrossMark

Nicolò Maccaferri,[1,a)] (ID) Tommi Isoniemi,[2,3] (ID) Michael Hinczewski,[4] (ID) Marzia Iarossi,[2,5] Giuseppe Strangi,[4,6,b)] (ID) and Francesco De Angelis[2] (ID)

AFFILIATIONS

[1] Department of Physics and Materials Science, University of Luxembourg, L-1511 Luxembourg, Luxembourg
[2] Istituto Italiano di Tecnologia, I-16163 Genova, Italy
[3] Department of Physics and Astronomy, University of Sheffield, Sheffield S3 7RH, United Kingdom
[4] Department of Physics, Case Western Reserve University, Cleveland, Ohio 44106, USA
[5] Dipartimento di Informatica, Bioingegneria, Robotica e Ingegneria dei Sistemi (DIBRIS), Università degli Studi di Genova, I-16126 Genova, Italy
[6] CNR-Nanotec e Dipartimento di Fisica, Università della Calabria, I-87036 Rende, Italy

[a)] Author to whom correspondence should be addressed: nicolo.maccaferri@uni.lu
[b)] giuseppe.strangi@case.edu

ABSTRACT

Hyperbolic metamaterials (HMMs) are anisotropic optical materials supporting highly confined propagating electromagnetic modes. However, it is challenging to tailor and excite these modes at optical frequencies by prism coupling because of the unavailability of high refractive index prisms for matching the momentum between the incident light and the guided modes. Here, we report on the mechanism of excitation of high-index Bloch plasmon polariton modes with sub-diffraction spatial confinement using a meta-grating, which is a combined structure of a metallic diffraction grating and a type II HMM. We show how a one-dimensional plasmonic grating without any mode in the infrared spectral range, if coupled to an HMM supporting high-index modes, can efficiently enable the excitation of these modes via coupling to far-field radiation. Our theoretical predictions are confirmed by experimental reflection measurements as a function of angle of incidence and excitation wavelength. We introduce design principles to achieve a full control of high-index modes in meta-gratings, thus enabling a better understanding of light–matter interaction in this type of hybrid structure. The exploitation of the spectral response of these modes can find applications in bio-chemical sensing, integrated optics, and optical sub-wavelength imaging.

Manipulation of photons at the nanoscale, well beyond the diffraction limit of light,[1–4] has become a topic of great interest for prospects in real-life applications,[5] such as energy harvesting and photosensitive chemical reactions,[6–8] subwavelength waveguides,[9] nanocavity lasers,[10] opto-electronics,[11] biochemistry,[12] and nanomedicine.[13] Since the last decade, conventional metallic materials have been shaped with advanced nanofabrication techniques in order to create electromagnetically coupled nanostructured systems, dubbed meta-materials, whose peculiar optical properties arise from the sub-wavelength confinement of light.[14] In this framework, hyperbolic metamaterials (HMMs) have received great attention

from the photonics community due to their unusual optical properties.[15–17] HMMs have been shown to enable negative refraction,[18–21] resonant gain singularities,[22] nanoscale light confinement,[23] optical cloaking,[24] extreme biosensing,[25–27] nonlinear optical phenomena,[28] super resolution imaging and superlensing effects,[29,30] plasmonic-based lasing,[31] artificial optical magnetism,[32] full control of absorption and scattering channels on the nanoscale,[33,34] etc. They display a hyperbolic iso-frequency surface,[35–37] which originates from one of the principal components of their effective permittivity or permeability tensor, having the opposite sign to the other two principal components. When considering the permittivity tensor, HMMs can

be divided into two types: type I has one negative component and two positive ones. In contrast, a type II HMM has two negative components and one positive. In practical terms, type II appears as a metal in one plane and as a dielectric along the perpendicular axis, while type I is the opposite, that is metallic along one direction and an insulator in the plane. Such anisotropic materials can sustain propagating modes with very large wavevectors, having long lifetimes and propagation lengths in comparison to classic plasmonic materials,[38,39] leading to a strong Purcell enhancement of spontaneous radiation.[40,41] Beyond the so-called natural hyperbolic materials, it is possible to mimic hyperbolic properties, for instance of type II, by using a periodic stack of metallic and dielectric layers[42] that can support surface plasmons and guided optical modes with large wavevectors[43] and whose effective permittivities for different polarizations have different signs.[37,44]

In this work, we focus on a one-dimensional (1D) metallic diffraction grating [sketched in the left-panel of Fig. 1(a)], which has been coupled to an artificial HMM of type II made of alternating layers of Au and Al_2O_3 [depicted in the left-panel of Fig. 1(b)].
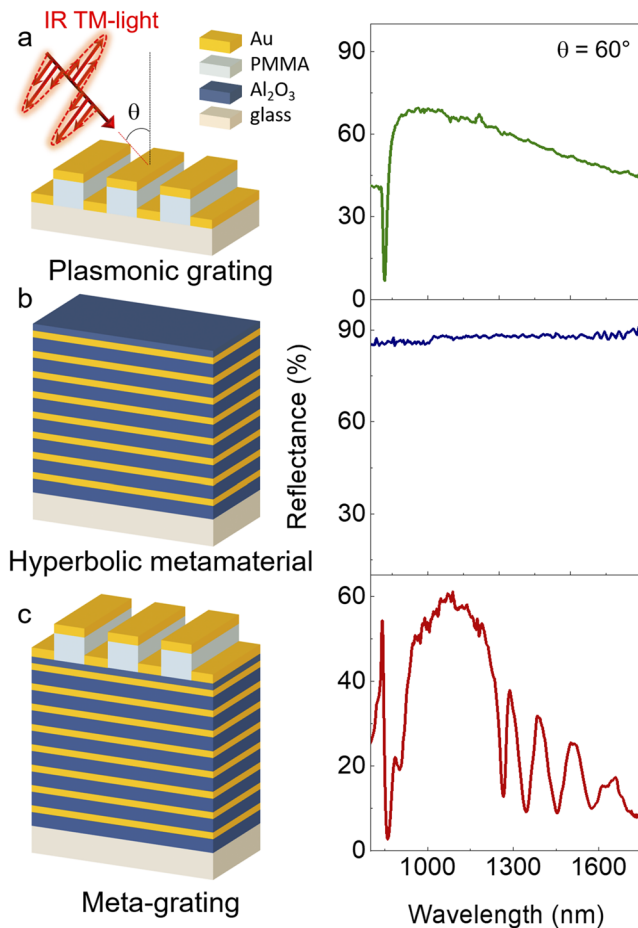

FIG. 1. Sketches of (a) the control 1D metallic grating, (b) the HMM, and (c) the meta-grating. On the right side of each sketch, specular reflectance spectra measured with TM-polarized light at incident angle θ = 60° are shown.

By using semi-analytical calculations, numerical simulations, and experiments, we provide a full overview of the main optical effects arising from the coupling between the 1D grating and a type II artificial HMM. We call this type of system "meta-grating," and a sketch of this architecture is presented in Fig. 1(c).

First, we consider a 1D metallic grating made of gold with a grating period of 450 nm, PMMA stripe dimensions of 250 nm (width) and 60 nm (thickness), and a 20 nm gold layer on top [Fig. 1(a)]. In the right panel of Fig. 1(a), we plot the experimental reflectance of this system, which has been fabricated by using a combination of e-beam evaporation and lithography techniques (see the supplementary material for more details) as a function of the wavelength of the incident transverse magnetic (TM, p-polarized) light at the representative incident angle θ = 60°. The choice of the angle is arbitrary; in our experimental setup the measurements can be performed at whatever angle between 15° and 75°. As can be seen by looking at the reflectance spectrum, no special features appear in the wavelength range 1000 nm–1750 nm. Similarly, if we consider the experimental reflectance of an HMM [Fig. 1(b)] made of eight alternating layers of Au (15 nm) and Al_2O_3 (30 nm) with an additional dielectric spacer (Al_2O_3, thickness 10 nm) on top, we can see that no features are present in the same spectral range [right panel of Fig. 1(b)]. Furthermore, the sample is highly reflective in the near-infrared region, as already demonstrated in previous works on similar systems.[45] Although the 1D metallic diffraction grating does not support any propagating plasmon in this range of wavelengths, the HMM can indeed support confined modes, which are not excitable by direct coupling of the HMM with external radiation. If we combine the 1D metallic grating and the HMM crystal, sharp and intense modes appear in the spectral region of interest [right panel of Fig. 1(c)].

It is important to note that with transverse electric (TE, s-polarized) incident light, no modes are observed in the meta-grating (see Fig. S1 of the supplementary material).

To get more physical insight into the observed effects, we have calculated, using a transfer matrix method (see the supplementary material for additional details), the dispersion of the modes that can be potentially excited in the HMM multilayer [Fig. 2(a)]. Under certain experimental conditions (such as the prism-coupling technique or high-energy electron beams), we can excite two Surface Plasmon Polariton (SPP) modes, indicated with S1 and S2, one at the interface with air and the other at the interface with the glass substrate, respectively. Nevertheless, these modes fall outside the spectral region we are interested in and are not the focus of this study. Interestingly, we can observe confined propagating modes, which are propagating within the multilayered structure. These modes, labeled Bn (where n = 1, 2, 3, . . .), are known as Bloch Plasmon Polaritons (BPPs) and are the eigenmodes of an HMM multilayer.[43] We now consider the dispersion relation of a diffraction grating, that is, $k_x = \Lambda \sin \theta + mG$, where $\Lambda = 2\pi/\lambda$ (λ is the wavelength of the incident light), $G = 2\pi/a$ (a is the grating period), θ is the angle of incidence, and m is an integer number, either positive or negative.[46,47] If we calculate the geometrical dispersion of a grating with period 450 nm and an angle of incidence of 60° for different values of m, for instance, −1, 1, and 2, we end up with the red lines in Fig. 2(a). As can be noticed, these curves intersect the BPP mode dispersion curves at precise energy values in the near-infrared spectral range, which we highlight with colored dots in Fig. 2(a). If we focus our attention on the grating
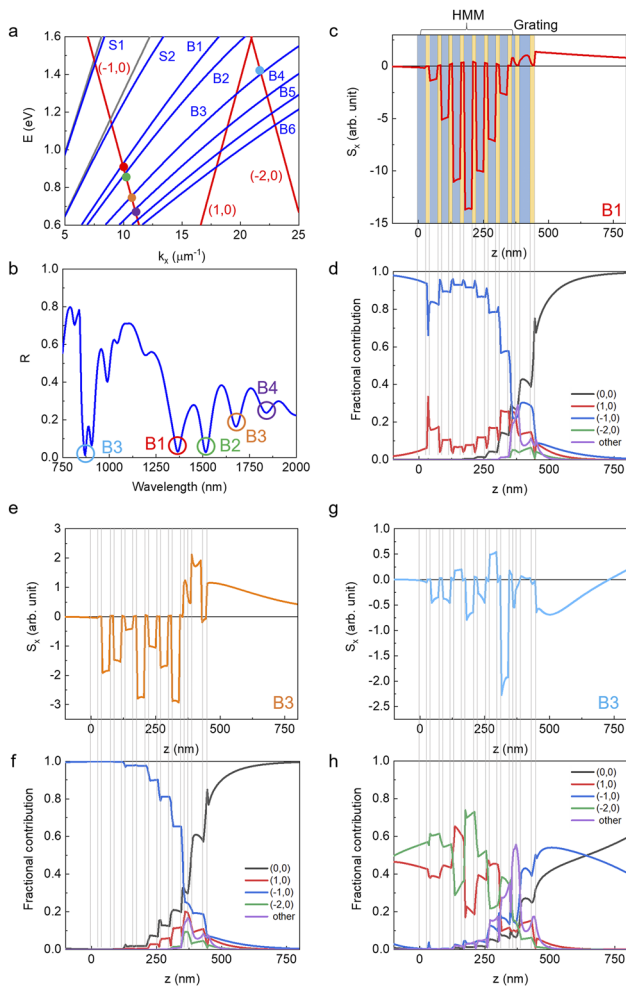
FIG. 2. Results of Fourier modal calculations for the meta-grating system. (a) Modal dispersion diagram in terms of incident light energy E vs transverse wavevector k_x. Thin blue lines are modes calculated for the HMM structure without the grating using the optical transfer matrix approach. The modes are labeled as follows: Sn (n = 1, 2) are SPPs and Bn (n = 1–6) are BPPs. The red dashed lines correspond to energy–wavevector relations for different diffraction orders: (−1, 0), (1, 0), and (−2, 0). The intersection of these relations and the energy at each minimum highlighted in panel (b) is shown as a colored dot. Note that the dots do not perfectly overlap with the calculated mode lines because the actual mode positions are shifted slightly in the presence of the grating. Curves corresponding to SPP propagation in air and glass are drawn in gray. (b) Reflectance vs wavelength for an angle of incidence of 60°. Three BPP modes (B1 at 1370 nm, B2 at 1520 nm, B3 at 870 nm and 1680 nm, and B4 at 1840 nm) are highlighted. For each of the modes B1 and B3 highlighted in panel (b), the transverse Poynting vector component vs height within the structure is shown in panels (c), (e), and (g). [(d), (f), and (h)] The corresponding fractional contribution of each diffraction order to the field within the structure. The dominant contributions are from orders (0, 0), (1, 0), (−1, 0), and (−2, 0). The other orders are summed together and labeled "other."

mode (−1, 0), we observe that it crosses the curves of the first four BPPs at 1370 nm (red dot—B1), 1520 nm (green dot—B2), 1680 nm (orange dot—B3), and 1840 nm (purple dot—B4). These results have also been confirmed through a scattering matrix method.[48] By

considering also the grating structure on top of the HMM multilayer, it results in the blue curve in Fig. 2(b), which reproduces well the experimental curve reported in the right panel of Fig. 1(c). The slight difference between the experimental and calculated spectral positions of the dips, as well as the relative spectral separation between them, is due to the difference in the values of the dielectric constants of the deposited materials and those used for the calculations.[49,50] Nevertheless, it is clear that our theoretical results and our simple argumentation (grating dispersion coupled to BPP dispersion) confirm the idea that the presence of a metallic diffraction grating on top of an HMM multilayer is responsible for the excitations of these modes in the near-infrared.

We also analyzed in detail how the different diffraction orders contribute to the excitation of these BPP modes. The B1 mode at 1370 nm [Fig. 2(c)] and the B3 mode at 1680 nm [Fig. 2(e)] are examples of the simplest scenario: one diffraction order is dominant throughout the interior of the HMM [see the (−1, 0) curve in Figs. 2(d) and 2(f)]. On the contrary, the mode B3 excited at 870 nm [Fig. 2(g)] is a bit more complicated because while the diffraction order (2, 0) is the largest contribution throughout most of the HMM, there is also a significant contribution coming from the diffraction order (1, 0). Thus, we get a mode with roughly the characteristics of B3 [compare Figs. 2(e) and 2(g)] based on the shape of the Poynting vector distribution [see the negative S_x peaks in the dielectric layers in Fig. 2(g)], but mixed with counter-propagating modes (positive peaks) excited via (1, 0). In this geometry and spectral range, the study-case "B3" is an important example of how the same BPP mode can be excited by using two different diffraction orders at two different wavelengths [see Figs. 2(a) and 2(e)–2(h)]. This result is also important since it demonstrates that by engineering the metallic diffraction grating geometry, one can achieve on-demand multiple excitations of the same mode, and thus of its peculiar field distribution, in different spectral ranges.

Although out of the scope of the current work, which is focused on the excitation of BPP modes by coupling with a metallic grating, it is worth noting that in Figs. 2(e)–2(h), an additional contribution coming from the diffraction mode (−1, 0) close to the multilayer/air interface is clearly present. This might come from the SPP mode excited by the grating at around 900 nm close to the B3 mode at 870 nm, which is clearly present also in the experimental curves shown in the right panels of Figs. 1(a) and 1(c).

After this analysis, we have performed angle and wavelength resolved experiments to prove the picture we have developed so far. In Fig. 3(a), we show a representative AFM (top panel) and SEM (bottom panel) image of a FIB-milled cross section on the experimentally realized meta-grating.

The experimental reflectance spectrum of the fabricated meta-grating as a function of the wavelength and the incident angle of the impinging TM-polarized far-field radiation is plotted in Fig. 3(b). Four dips are clearly visible in the studied spectral range. These modes are also highlighted with colored circles at θ = 60° (for more details about the optical measurements, see the supplementary material). Because the angle of incidence and the grating geometry are known, we were able to extract the real part of the effective index [phase velocity of the mode divided by the speed of light, see points in Fig. 3(c)] of each mode from the experimental reflectance measurements in Fig. 3(b). We have also made a direct comparison with our theory [see the colored lines in Fig. 3(c)], thus confirming that
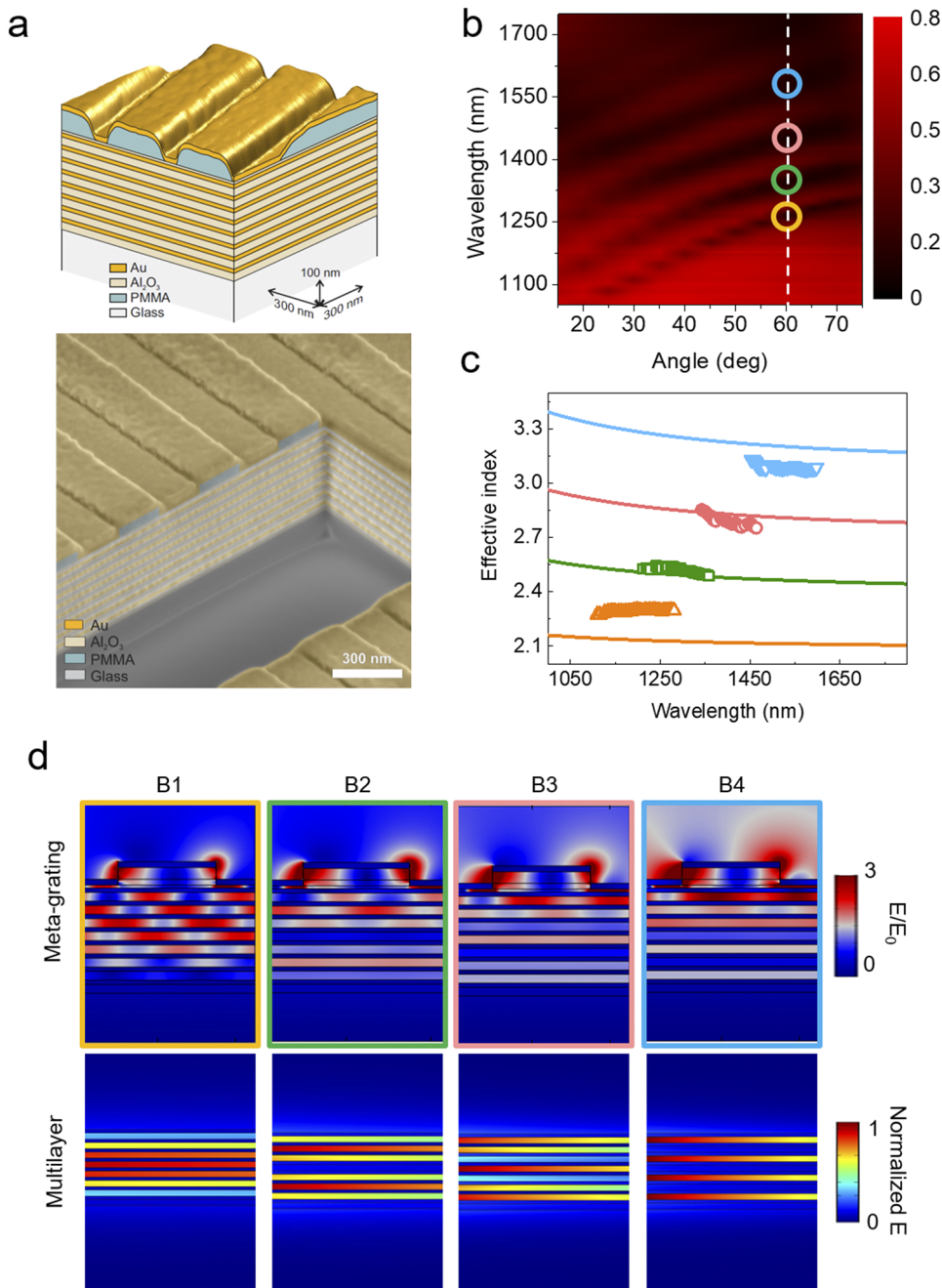
FIG. 3. (a) Top panel: colorized AFM image of the gold/PMMA grating surface (the rest of the figure is a sketch of the HMM multilayer). Bottom panel: colorized SEM image of a FIB trench on the metallic grating made of PMMA (60 nm thick) on an HMM multilayer covered with 20 nm of Au. (b) Experimental reflectance as a function of the wavelength and the incident angle of the incoming TM-polarized light. The four BPP modes excited in the meta-grating at θ = 60° are highlighted with colored circles. (c) Experimental (dots) and calculated (lines) effective refractive index of the four BPP modes. (d) Top panel: near-field distribution of the four BPP modes that are excited in the meta-grating. Bottom panel: exact solution of the electromagnetic field distribution of an HMM on a glass substrate without the metallic grating on top obtained via finite element method-based mode analysis.

the excited BPPs are high-index modes (n > 2) and that at each mode, they correspond to a specific modal index.

We also performed an alternative mode analysis, based on the finite element method (see the supplementary material for more details), to further support the results of our semi-analytical modeling developed so far. In the top panels of Fig. 3(d), we have plotted the near-field distribution of the first four BPP modes excited with TM-polarized light at θ = 60° by using the same geometrical parameters of the fabricated structures. As can be inferred by looking at the field distributions within the HMM plotted in these four panels, the peculiar field distributions we have found by using the transfer matrix method appear at the wavelengths where the grating mode crosses the BPP modes. These are exactly the field distributions we obtained by solving numerically the eigenvalue problem of a multilayered HMM on a glass substrate without the diffraction grating on top of it [bottom panels of Fig. 3(d)], which also perfectly

match the distribution of the Poynting vector obtained by using the transfer matrix approach used in Figs. 2(c)–2(h). This proves that although no SPP modes are supported by the diffraction metallic grating in this wavelength range, the presence of a diffraction order allows the excitation of the BPP modes, which cannot be excited by directly coupling the far-field infrared radiation with the multilayer in the absence of the grating itself. If we look at Fig. 3(d), we can also observe that the field distribution at the grating level is almost the same for all four the cases, indicating that (i) it is only one grating mode, which is actually contributing to the excitation of the BPP modes (thus confirming the diffraction orders' contribution analysis made in Fig. 2) and (ii) the mode is almost localized.

To prove the latter hypothesis, we have also calculated the reflectance of four meta-gratings where we considered different types of gratings on top of the HMM. In Fig. 4(a), we plot the four geometries considered (included the one used in the experiments), along with the calculated reflectance spectra at $\theta = 60°$ and the near-field distributions for a representative mode, in this case, the B2 mode. The choice of this mode is arbitrary, and the same analysis can be applied to all the other three modes studied here. By directly comparing the response of the four meta-grating cases presented in Fig. 4, it turns out that it is a localized diffraction mode at the thin Au stripe edges, which is the main responsible for the excitation of the BPP modes. Moreover, by comparing the responses of the Au grating on top of PMMA stripes with a dielectric spacer (simulation of the experimental case—top-left panel) and the case of the Au layer on top of the PMMA stripe (top-right panel), it is clear that the underlying gold layer is also important, since the absorption efficiency is maximized only in this case. We then considered an ideal grating, namely, a grating made of pure gold (bottom-left panel) and also an Au thin film with a stripe etched within it (anti-stripe geometry, bottom-right panel), and again we can excite the B2 mode, although in these two cases, the efficiency is very low. All these observations become clearer by looking at Fig. 4(b), where we plot the related calculated absorption efficiencies in the wavelength range where the B2 mode is excited using these four different diffraction gratings. By playing with the grating geometry, we can either achieve a negligible absorption (pure gold grating case) or a huge absorption (>99%) in the case of the Au film deposited on top of a PMMA stripe, which is the same for our experimental case, although there we reach an absorption efficiency of ≈90% mostly due to structural defects. Similar effects were also recently observed in the visible spectral region by Azzam *et al.* who studied the formation of hybrid photonic-plasmonic modes when coupling a 1D metallic grating with a dielectric optical waveguide.[51] In that study, the plasmonic propagating modes can be excited directly by coupling with far-field radiation, and they hybridize with the cavity modes in the waveguide, while in our case, it is crucial to couple the two systems, which are not displaying any plasmonic mode (in the case of the grating) or bright mode (in the case of the HMM) if taken separately.

After this analysis, we have also studied, from a pure numerical point of view, how the thickness of some important components of either the HMM multilayer or the grating on top of it can affect the dispersion of the modes. We focused our parametric study on the role played by the thickness of the PMMA bar, the Al_2O_3 spacer, and the metal/dielectric layers. In Fig. 5, we display the calculated reflectance of the meta-grating as a function of the wavelength of the
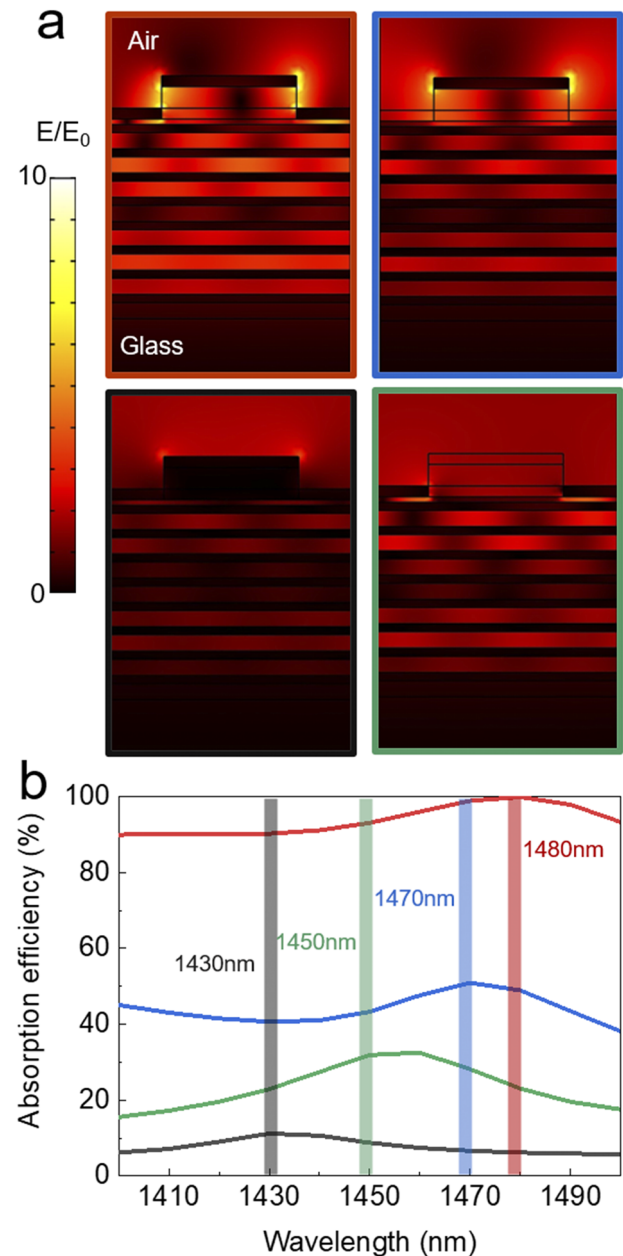

FIG. 4. (a) Calculated near-field distribution of the B2 mode excited in four different meta-gratings: experimental case (top-left), namely, a PMMA stripe with a gold thin film (thickness 20 nm) on top, a gold stripe on top of a PMMA bar, and no gold on top of the dielectric spacer (top-right), a pure gold grating (bottom-left), and an anti-stripe geometry (bottom-right), namely, a gold film with a stripe etched on it. The excitation wavelengths of the B2 mode in each case are marked in panel (b), which shows the corresponding calculated absorption efficiencies.

incident light (for $\theta = 60°$) and the thickness of the Al_2O_3 layers. We maintained fixed the value of the thickness of the Au layers in each panel, and we considered four different Au thicknesses (5 nm, 15 nm, 25 nm, and 35 nm, the latter comparable with the skin depth
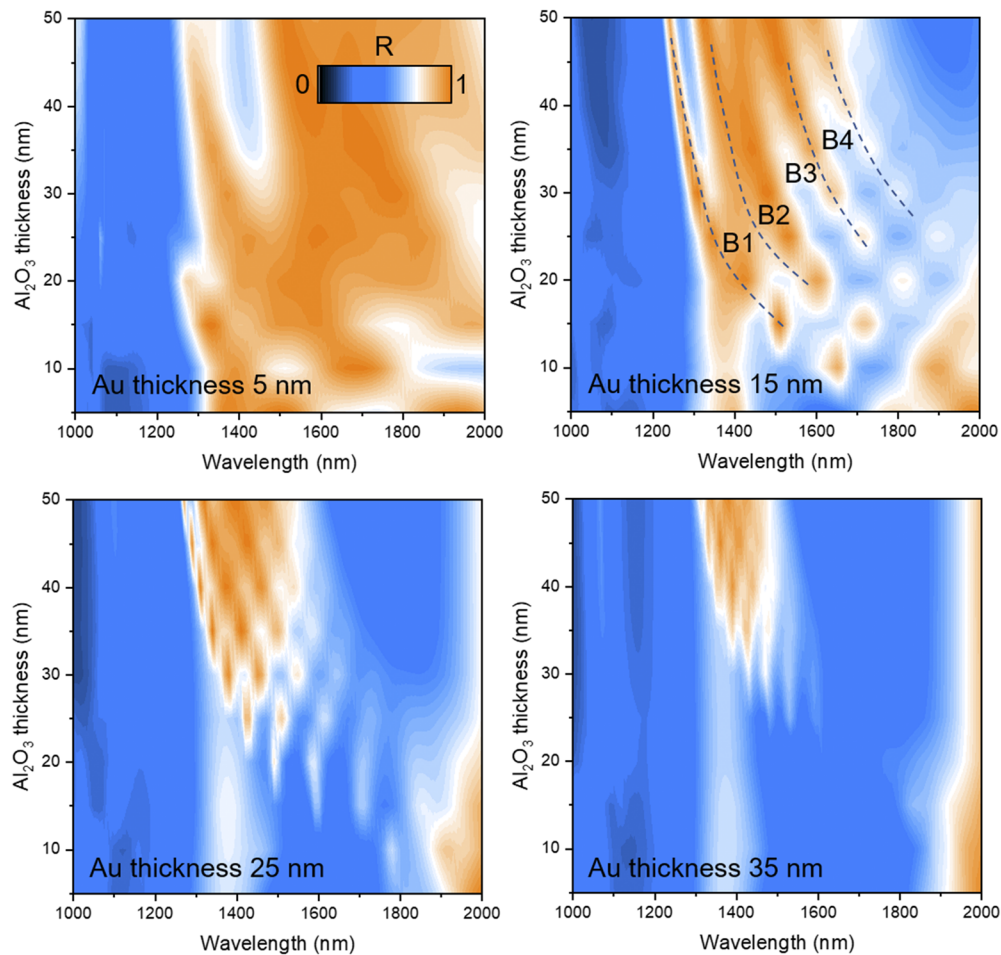
FIG. 5. Calculated reflectance of a meta-grating as a function of the Al$_2$O$_3$ thickness in the repeated multilayer and the wavelength of the impinging light. In each panel, the thickness of the Au layers has been changed from 5 nm (top left panel) to 35 nm (bottom right panel). The blue dashed lines are guidelines to the eyes to help the reader visualizing the BPP modes' reflectance dependence on the wavelength and Al$_2$O$_3$ thickness.

of gold in the near-infrared). As can be seen, there is a threshold dictated by the experimental value of 15 nm, above which the four BPP modes merge and disappear. Moreover, already for an Au thickness of 25 nm, the intensity of these four modes strongly drops for values of the Al$_2$O$_3$ thickness below 30 nm. We then calculated the dependence of the BPP mode dispersion on the PMMA bar and Al$_2$O$_3$ spacer thicknesses. We left the Au film thickness constant and equal to 20 nm in all the cases. In Fig. 6, we report the reflectance of the meta-grating for θ = 60° and for different values of the PMMA bar thickness as a function of the wavelength of the incident light and of the Al$_2$O$_3$ spacer thickness. As can be inferred from the plotted maps, to achieve a proper coupling between the metallic grating and the HMM multilayer, the PMMA bar thickness has to be larger than the Au film thickness, that is, we need to separate well the top part of the grating from its bottom part. Indeed, only for thicknesses above 40 nm, we start to see the appearance of the four BPP modes. It is also interesting to note that for PMMA bar thicknesses above 60 nm (as

in the experimental case), the dispersion of the four BPP modes is not strongly modified.

Moreover, it is also important to note that the Al$_2$O$_3$ spacer thickness should not be larger than 20 nm–30 nm because for thicknesses larger than this value, the reflectance dips become less intense, which is a signature that the coupling between the grating and the HMM multilayer is not optimal. Nevertheless, keeping a larger spacer thickness might be useful for achieving a sharper mode width, thus a better quality factor.

The two analyses we have done so far are important since they show how, by playing with either the geometry of the grating or the thickness of the HMM layers, we can tune the spectral distance, the position, and the intensity of the modes (see Figs. 4 and 5). Moreover, it is worth mentioning that a geometry-dependent width of the modes, as shown in Figs. 5 and 6, has an important repercussion on the quality factor of the resonant mode. Consequently, the Purcell factor of an emitter placed either inside or close to the cavity can
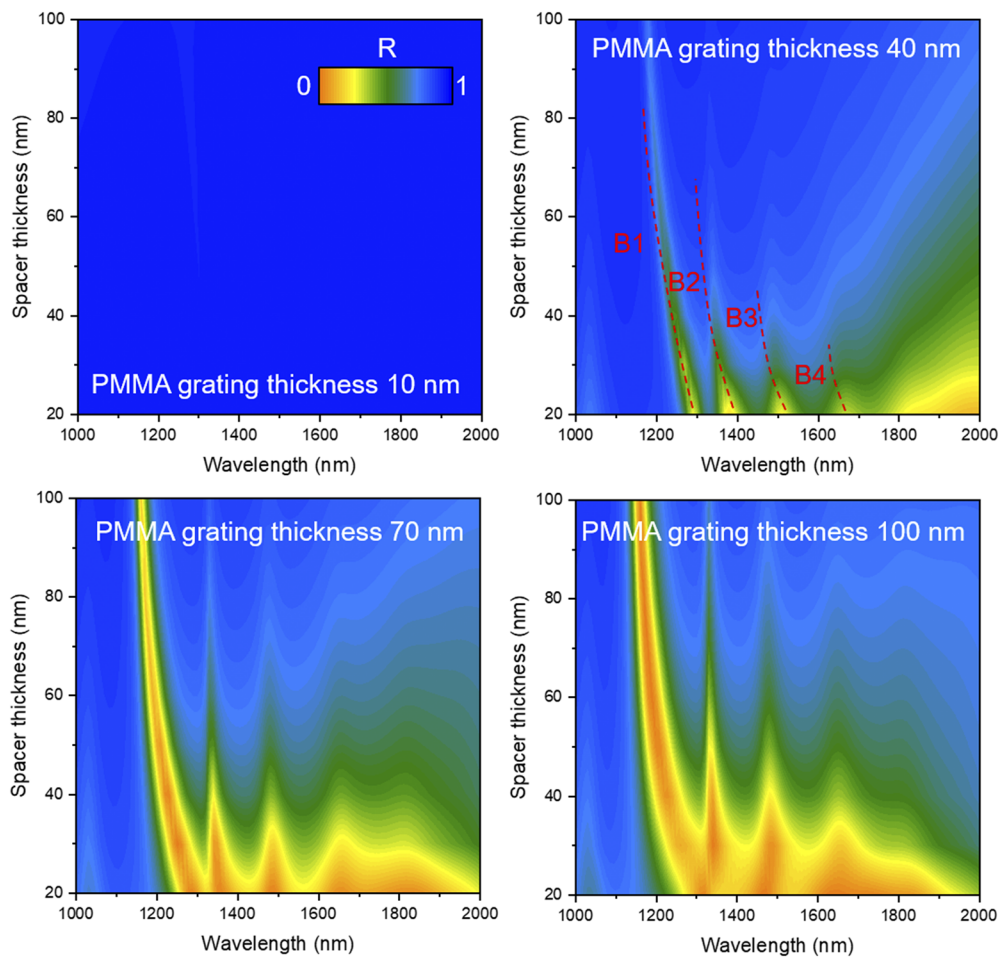
FIG. 6. Calculated reflectance of a meta-grating as a function of the Al_2O_3 spacer thickness and the wavelength of the impinging light, where the thickness of the PMMA bar has been changed from 10 nm to 100 nm. The red dashed lines are guidelines to the eyes to help the reader visualizing the BPP modes' reflectance dependence on the wavelength and Al_2O_3 spacer thickness.

be strongly modified by the interaction with a specific BPP mode. Depending on the quality factor of such a mode, one can obtain a tailored modulation of the Purcell factor of the emitter and manipulate its emission properties.[40,41,52–55]

Finally, as already shown in Fig. 3(c), it is also important to note that the BPP modes supported by the HMM multilayer display different refractive indices depending on the order of the mode.[43] These indices are known as modal indices and affect both the propagation and penetration distance of the confined BPP waves within the multilayer. In Figs. 7(a) and 7(b), we report the calculated real and imaginary part, respectively, of the modal index of the first seven modes supported by the HMM for the representative wavelength of 1500 nm. It is important to notice that although the absolute values might change by considering different wavelengths, the overall trend, which is monotonic in the spectral region where the HMM shows a hyperbolic dispersion [see also Fig. 3(c)], is the same. As the number of the mode increases, also the losses [plotted in Fig. 7(c)]

increase. For comparison, we also plot the calculated modal indexes, along with the other quantities, of the two SPP modes at the air and glass interfaces (blue and yellow lines, respectively). By increasing the modal index, we can also slow down radiation velocity [see Fig. 7(d)] within the structure. This is an important feature in view of practical photonic applications where tunable lifetimes are needed on the same platform, and our architecture might represent an interesting candidate to achieve this functionality. Finally, it is worth mentioning here that high-index and slow photonics modes like these can be used for enhancing nonlinear interactions as well as in optical circuitry, especially for buffering, switching, and time-domain processing of optical signals.[56–58]

In conclusion, we have demonstrated the excitation mechanism of Bloch Plasmon Polariton modes in the near-infrared using a meta-grating approach, that is a metallic diffraction grating coupled to an artificial hyperbolic material of type II. Due to the coupling between the dark Bloch modes supported by the multilayered
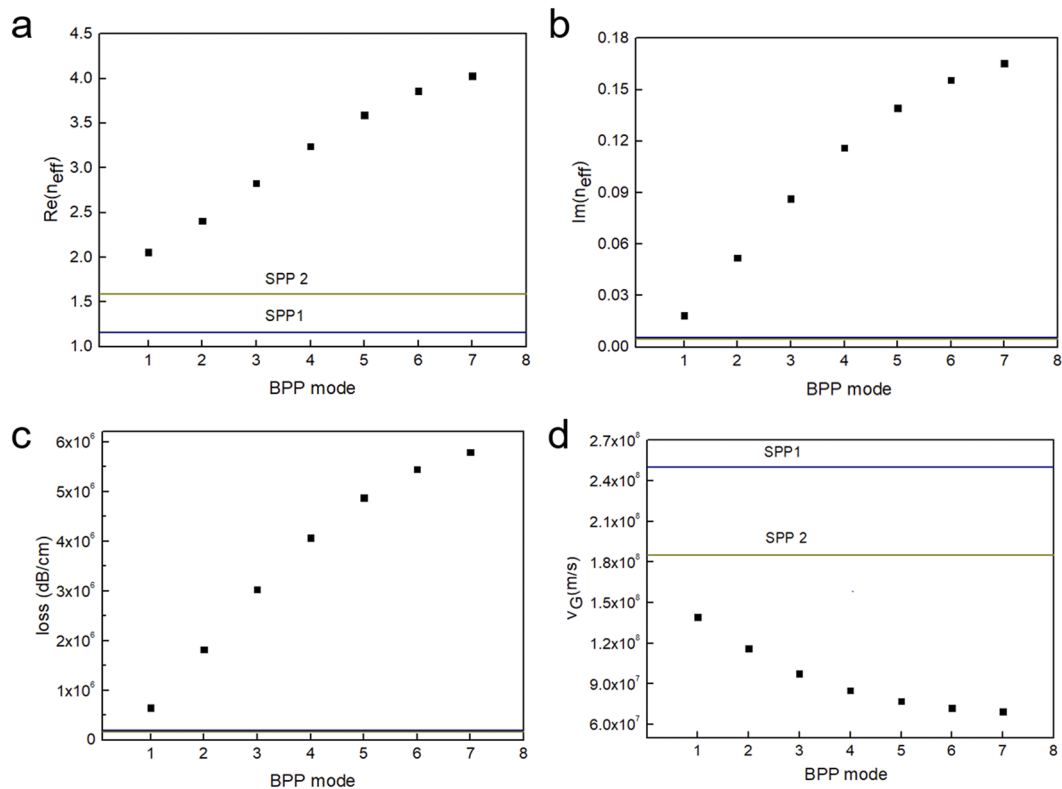
FIG. 7. Calculated real (a) and imaginary (b) parts of modal indices, and (c) losses and (d) group velocities for the seven BPP modes supported by an 8-bilayer HMM at the representative wavelength of 1500 nm.

hyperbolic structure and the diffraction modes of the grating, the nature of the modes is exchanged at given spectral points, giving rise to sharp modes with geometry-tailored quality factor and tunable spectral position, lifetimes, and group velocities. These modes are characterized by high absorption efficiency (>99%) in the near-infrared spectral region, making them perfect candidates for applications in tunable-threshold lasers, sharp spectral filters, perfect absorbers, enhancement of nonlinear phenomena, and biochemical sensors.

See the supplementary material for methods such as sample fabrication, optical measurements, and numerical simulations and for the angular dependence of the meta-grating for TE-polarized incident light.

AUTHORS' CONTRIBUTIONS

All the authors contributed to the study and the writing of the manuscript. N.M. and M.H. developed the theory and performed the semi-analytical and numerical calculations and data analysis. T.I. fabricated the samples and measured the reflectance spectra. M.I. helped with the data analysis. G.S. and F.D.A. supervised the work. N.M., T.I., and M.H. contributed equally to this work.

DATA AVAILABILITY

The data that support the findings of this study are available from the corresponding authors upon reasonable request.

REFERENCES

[1] S. Meyer, *Plasmonics: Fundamental and Applications* (Springer, 2007).
[2] W. L. Barnes, A. Dereux, and T. W. Ebbesen, Nature **424**, 824 (2003).
[3] P. Muhlschlegel *et al.*, Science **308**, 1607 (2005).
[4] H. A. Atwater Sci. Am. **296**, 56–62 (2007).
[5] S. Lal, S. Link, and N. Halas, Nat. Photonics **1**, 641–648 (2007).
[6] V. E. Ferry, L. A. Sweatlock, D. Pacifici, and H. A. Atwater, Nano Lett. **8**, 4391–4397 (2008).
[7] O. Neumann, C. Feronti, A. D. Neumann, A. Dong, A. Schell, B. Lu, E. Kim, M. Quinn, S. Thompson, N. Grady *et al.*, Proc. Natl. Acad. Sci. U. S. A. **110**, 11677–11681 (2013).
[8] F. Dayne *et al.*, Proc. Natl. Acad. Sci. U. S. A. **113**, 8916–8920 (2016).

[9]H. Altug, D. Englund, and J. Vučković, Nat. Phys. **2**, 484–488 (2006).

[10]S. I. Bozhevolnyi, V. S. Volkov, E. Devaux, J.-Y. Laluet, and T. W. Ebbesen, Nature **440**, 508–511 (2006).

[11]S. Lei, F. Wen, L. Ge, S. Najmaei, A. George, Y. Gong, W. Gao, Z. Jin, B. Li, J. Lou et al., Nano Lett. **15**, 3048–3055 (2015).

[12]R. Bardhan, W. Chen, M. Bartels, C. Perez-Torres, M. F. Botero, R. W. McAninch, A. Contreras, R. Schiff, R. G. Pautler, N. J. Halas, and A. Joshi, Nano Lett. **10**, 4920–4928 (2010).

[13]C. Ayala-Orozco, C. Urban, M. W. Knight, A. S. Urban, O. Neumann, S. W. Bishnoi, S. Mukherjee, A. M. Goodman, H. Charron, T. Mitchell et al., ACS Nano **8**, 6372–6381 (2014).

[14]N. Yu and F. Capasso, Nat. Mater. **13**, 139–150 (2014).

[15]A. Poddubny, I. Iorsh, P. Belov, and Y. Kivshar, Nat. Photonics **7**, 948–957 (2013).

[16]E. E. Narimanov and A. V. Kildishev, Nat. Photonics **9**, 214–216 (2015).

[17]O. Hess et al., Nat. Mater. **11**, 573–584 (2012).

[18]J. B. Pendry, Phys. Rev. Lett. **85**, 3966–3969 (2000).

[19]R. A. Shelby, D. R. Smith, and S. Schultz, Science **292**, 77–79 (2001).

[20]J. Valentine et al., Nature **455**, 376–379 (2008).

[21]S. Xiao et al., Nature **466**, 735–738 (2010).

[22]V. Caligiuri, L. Pezzi, A. Veltri, and A. De Luca, ACS Nano **11**, 1012–1025 (2017).

[23]L. Novotny and N. van Hulst, Nat. Photonics **5**, 83–90 (2011).

[24]W. Cai, U. K. Chettiar, A. V. Kildishev, and V. M. Shalaev, Nat. Photonics **1**, 224–227 (2007).

[25]A. V. Kabashin et al., Nat. Mater. **8**, 867–871 (2009).

[26]K. V. Sreekanth, Y. Alapan, M. ElKabbash, E. Ilker, M. Hinczewski, U. A. Gurkan, A. De Luca, and G. Strangi, Nat. Mater. **15**, 621–627 (2016).

[27]G. Palermo, G. E. Lio, M. Esposito, L. Ricciardi, M. Manoccio, V. Tasco, A. Passaseo, A. De Luca, and G. Strangi, ACS Appl. Mater. Interfaces **12**(27), 30181–30188 (2020).

[28]B. Wells, Z. A. Kudyshev, N. Litchinitser, and V. A. Podolskiy, ACS Photonics **4**, 2470–2478 (2017).

[29]Z. Liu et al., Science **315**, 1686 (2007).

[30]Q. Ma, H. Qian, S. Montoya, W. Bao, L. Ferrari, H. Hu, E. Khan, Y. Wang, E. E. Fullerton, E. E. Narimanov, and X. Zhang, ACS Nano **12**(11), 11316–11322 (2018).

[31]T. Galfsky, Z. Sun, C. R. Considine, C.-T. Chou, W.-C. Ko, Y.-H. Lee, E. E. Narimanov, and V. M. Menon, Nano Lett. **16**, 4940–4945 (2016).

[32]G. T. Papadakis, D. Fleischman, A. Davoyan, P. Yeh, and H. A. Atwater, Nat. Commun. **9**, 296 (2018).

[33]N. Maccaferri, Y. Zhao, T. Isoniemi, M. Iarossi, A. Parracino, G. Strangi, and F. De Angelis, Nano Lett. **19**, 1851–1859 (2019).

[34]T. Isoniemi, N. Maccaferri, Q. M. Ramasse, G. Strangi, and F. De Angelis, Adv. Opt. Mater. **8**(13), 2000277 (2020).

[35]S. A. Biehs and M. Tschikin, Phys. Rev. Lett. **109**, 104301 (2012).

[36]D. R. Smith and D. Schurig, Phys. Rev. Lett. **90**, 077405 (2003).

[37]T. Li and J. B. Khurgin, Optica **3**, 1388–1396 (2016).

[38]P. Li et al., Science **359**, 892–896 (2018).

[39]X. Yang, J. Yao, J. Rho, X. Yin, and X. Zhang, Nat. Photonics **6**, 450–454 (2012).

[40]D. Lu et al., Adv. Mater. **30**, 1706411 (2018).

[41]D. Lu, J. J. Kan, E. E. Fullerton, and Z. Liu, Nat. Nanotechnol. **9**, 48–53 (2014).

[42]N. Liu et al., Nat. Mater. **7**, 31–37 (2008).

[43]I. Avrutsky, I. Salakhutdinov, J. Elser, and V. Podolskiy, Phys. Rev. B **75**, 241402(R) (2007).

[44]F. Peragut et al., Optica **4**, 1409–1415 (2017).

[45]K. V. Sreekanth, A. De Luca, and G. Strangi, Sci. Rep. **3**, 3291 (2013).

[46]Diffraction Gratings, edited by M. C. Hutley (Academic Press, 1982).

[47]Electromagnetic Theory of Gratings, edited by R. Petit (Springer-Verlag Berlin Heidelberg, 1980).

[48]N. Anttu and H. Q. Xu, Phys. Rev. B **83**, 165431 (2011).

[49]A. D. Rakić, A. B. Djurišic, J. M. Elazar, and M. L. Majewski, Appl. Opt. **37**, 5271–5283 (1998).

[50]R. Boidin, T. Halenkovič, V. Nazabal, L. Beneš, and P. Němec, Ceram. Int. **42**, 1177–1182 (2016).

[51]S. I. Azzam, V. M. Shalaev, A. Boltasseva, and A. V. Kildishev, Phys. Rev. Lett. **121**, 253901 (2018).

[52]C. Guclu, T. S. Luk, G. T. Wang, and F. Capolino, Appl. Phys. Lett. **105**, 123101 (2014).

[53]S. R. K. C. Indukuri, J. Bar-David, N. Mazurski, and U. Levy, ACS Nano **13**(10), 11770–11780 (2019).

[54]V. Caligiuri, G. Biffi, M. Palei, B. Martín-García, R. D. Pothuraju, Y. Bretonnière, and R. Krahne, Adv. Opt. Mater. **8**(1), 1901215 (2020).

[55]G. Palermo, G. E. Lio, and G. Strangi, Quantum Stud.: Math. Found. (published online 2020).

[56]T. F. Krauss, Nat. Photonics **2**(8), 448 (2008).

[57]A. R. Rashed, B. G. Yildiz, S. R. Ayyagari, and H. Caglayan, Phys. Rev. B **101**, 165301 (2020).

[58]J. Kuttruff, D. Garoli, J. Allerbeck, R. Krahne, A. De Luca, D. Brida, V. Caligiuri, and N. Maccaferri, Commun. Phys. **3**, 114 (2020).